

S²RC-GCN: A Spatial-Spectral Reliable Contrastive Graph Convolutional Network for Complex Land Cover Classification Using Hyperspectral Images

1st Renxiang Guan

*School of Computer
China University of Geosciences
Wuhan, China
grx1126@cug.edu.cn*

3st Chujia Song

*School of Geography and Information Engineering
China University of Geosciences
Wuhan, China*

5st Xianju Li*

*School of Computer
China University of Geosciences
Wuhan, China
ddwhlxj@cug.edu.cn*

2st Zihao Li

*School of Computer
China University of Geosciences
Wuhan, China*

4st Guo Yu

*School of Management
Wuhan University of Science and Technology
Wuhan, China*

6st Ruyi Feng

*School of Computer
China University of Geosciences
Wuhan, China*

Abstract—Spatial correlations between different ground objects are an important feature of mining land cover research. Graph Convolutional Networks (GCNs) can effectively capture such spatial feature representations and have demonstrated promising results in performing hyperspectral imagery (HSI) classification tasks of complex land. However, the existing GCN-based HSI classification methods are prone to interference from redundant information when extracting complex features. To classify complex scenes more effectively, this study proposes a novel spatial-spectral reliable contrastive graph convolutional classification framework named S²RC-GCN. Specifically, we fused the spectral and spatial features extracted by the 1D- and 2D-encoder, and the 2D-encoder includes an attention model to automatically extract important information. We then leveraged the fused high-level features to construct graphs and fed the resulting graphs into the GCNs to determine more effective graph representations. Furthermore, a novel reliable contrastive graph convolution was proposed for reliable contrastive learning to learn and fuse robust features. Finally, to test the performance of the model on complex object classification, we used imagery taken by Gaofen-5 in the Jiang Xia area to construct complex land cover datasets. The test results show that compared with other models, our model achieved the best results and effectively improved the classification performance of complex remote sensing imagery.

Index Terms—Contrastive learning, hyperspectral image, graph convolutional network, land cover classification

I. INTRODUCTION

Land cover information is important for studying biodiversity, human-land relationships, and other issues, as it is a crucial component in resource utilization and environmental protection [1], [2]. The rapid development of imaging spectroscopy technology probabilizes fine-grained land cover classification (FLCC), and many algorithms work to complete the mapping from remote sensing imagery to pixel-wise labels of land cover [3], [4]. Specifically, conducting FLCC

in complex geographical scenarios is advantageous because of the rich spectral information [5], [6], [7], [8]. However, with the gradual improvement in the spectral resolution of hyperspectral image (HSI), the intracategory differences of the same type of ground objects and the redundancy of spectral features have represented severe challenges to FLCC [9], [10], [11], [12], [13].

Deep learning (DL)-based algorithms can extract robust deep features layer by layer and are gaining considerable attention in the field of HSI processing [14], [15], [16], [17]. As typical DL models, convolutional neural networks (CNNs) are widely used to solve HSI classification problems [18], ranging from 1D-CNN to 3D-CNN [19], [20], [21], [22], [23], [24]. Hu et al. [19] first proposed a 1D-CNN to extract the pixel spectral features. To capture spatial features, Chen et al. [20] designed a 2D-CNN model that employed several convolution and pooling layers to obtain nonlinear deep features and used them for HSI classification. Rasti et al. [25] proposed a three-stream CNN for LCC using HSI and LIDAR data. In addition, residual networks (ResNets) [26], dense networks [27] and Capsule network [28] have been introduced into HSI tasks and have demonstrated strong performance. However, these methods only focus on extracting image region features with a fixed kernel size, thereby ignoring the long-range spatial relationships of different local regions [29], [30], [31], [32], [33].

To address the disadvantages of CNN, graph convolutional networks (GCNs) have been applied to HSI classification tasks, which can convolve arbitrarily structured graphs and preserve class boundary information [34], [35], [36]. Ma et al. [37] first combined spectral and spatial regularization to propose a graph-based semi-supervised spatial-spectral joint feature HSI classification method. Qin et al. [38] proposed a new framework for semi-supervised learning based on a GCN

*Corresponding author

that considers both the spatial and spectral features of HSI in the filtering operation of the graph. However, semi-supervised tasks must consider the spatial relationship between all pixels, which incurs a high computational cost. In response to this problem, Wan et al. [39] used the SLIC [40] algorithm to segment an image into superpixels and used them as the nodes of the graph while dynamically updating the graph structure using the graph convolution process. Liu et al. [41] used a GCN to learn superpixel features, a CNN to learn pixel-level features, and ultimately fused the features. However, these methods use full-batch network learning, which incurs huge memory overhead. In response, Hong et al. [42] proposed a mini-batch GCN to integrate the features of a GCN and a CNN in an end-to-end trainable network. Subsequently, an increasing number of methods based on GCN have been introduced into HSI classification research, such as the hypergraph [43] and spatial-pooling GCN [44].

To enhance the robustness of feature learning, contrastive learning has been incorporated into HSI processing tasks. Huang et al. [45] introduced an innovative approach called 3D swin transformer-based hierarchical contrast learning, which effectively leveraged the multi-scale semantic representation of an image. Lu et al. [46] proposed a novel end-to-end supervised contrastive learning network for spectral-spatial classification. Guan et al. [47] proposed a contrastive subspace clustering method based on GCN. Yu et al. [48] devised a semi-supervised contrastive loss to exploit the supervision contained in the spectral signatures of image regions [49], [50], [51].

Nevertheless, current GCN-based contrastive methods still contain some disadvantages. On the one hand, the positive samples generated by these methods are typically limited to one, whereas negative samples are randomly chosen, introducing a certain level of randomness and the potential for misclassification. This randomness diminishes the model's capability to extract features to some extent [52], [53], [54]. Therefore, it is imperative to develop a reliable contrastive method during feature propagation between adjacent layers of a GCN. On the other hand, an adjacency matrix is known to represent the topology of the graph data [55], [56]. However, most GCN-based methods use only the shallow spatial or spectral information of HSI to construct graphs, which can only represent pairwise relationships and cannot discover the underlying complex structures in the complete land cover imagery [57], [58], [59].

To alleviate these deficiencies, we propose a novel spatial-spectral reliable contrastive graph convolutional network (S^2RC -GCN) for complex land cover classification. In the model, 1D-encoder and 2D-encoder learn high-level spectral and spatial features respectively from HSI to further construct deep graphs, and then feed the generated graphs into GCN for further classification tasks. In particular, we propose a reliable contrastive GCN, which uses nodes with true labels or predictive labels with high thresholds for contrastive learning to further learn more efficient graph representations. To test the effectiveness of the model in complex ground object

classification tasks, this paper uses two complex land cover datasets captured by the Gaofen-5 satellite (GF-5) and a general dataset. The main contributions of this paper are as follows:

- 1) This paper designs a new CNN-GCN framework named S^2RC -GCN. It fuses spatial and spectral features by 1D-encoder and 2D-encoder, and 2D-encoder includes an attention model to automatically extract important information which can effectively capture deep features for robust graph construction.
- 2) The supervised contrastive loss and the enhancement of reliable samples are crafted to leverage the supervision signals inherent in the HSI, avoiding the noise introduced by the data augmentation process.
- 3) To better test the robustness and generalizability of the model, the paper uses two complex land cover datasets captured by the GF-5 and a general HSI dataset.

II. METHOD

A flowchart of the proposed S^2RC -GCN system is shown in the Figure 1. In this section, we introduce the details of each part and illustrate the implementation. We first introduce the basic feature extraction model included in the algorithm; then the patch-level spatial information and pixel-level spectral information are extracted and fused; the third section introduces how to use the fused features and spectral features to construct robust graph adjacency matrices; Afterward, the fourth section details the construction of reliable contrastive graph convolution.

A. Basic Model

2D-CNN (SE-ResNet): Because the CNN uses a convolution kernel to fuse the spatial information on the local receptive field and the information on the channel dimension to construct the feature map, it causes multiple problems simultaneously [60], [61]. Different feature channels are further used with equally important weights to create global irrelevance, and the features are propagated through the network, thus affecting their accuracy. Therefore, the feature extraction network designed in this study is SE-ResNet. Before Squeeze-and-Excitation model is applied, we use the principal component analysis (PCA) [62] to reduce the band dimension of HSI to reduce redundant spectral information. Figure 2 shows a schematic of the SE-ResNet network structure. SE-Net is implemented in two steps: 1) global information embedding and 2) adaptive rescaling. In global information embedding, the output of the CNN compresses the features along the spatial dimension through the global pooling layer. In adaptive rescaling, a gate with a sigmoid activation function is selected to obtain a normalized weight between zero and one, which is the scale weight factor used to characterize the importance of each channel. Finally, the normalized weights were assigned to the features of each channel through a scale operation to complete the recalibration of the original features in the channel dimension.

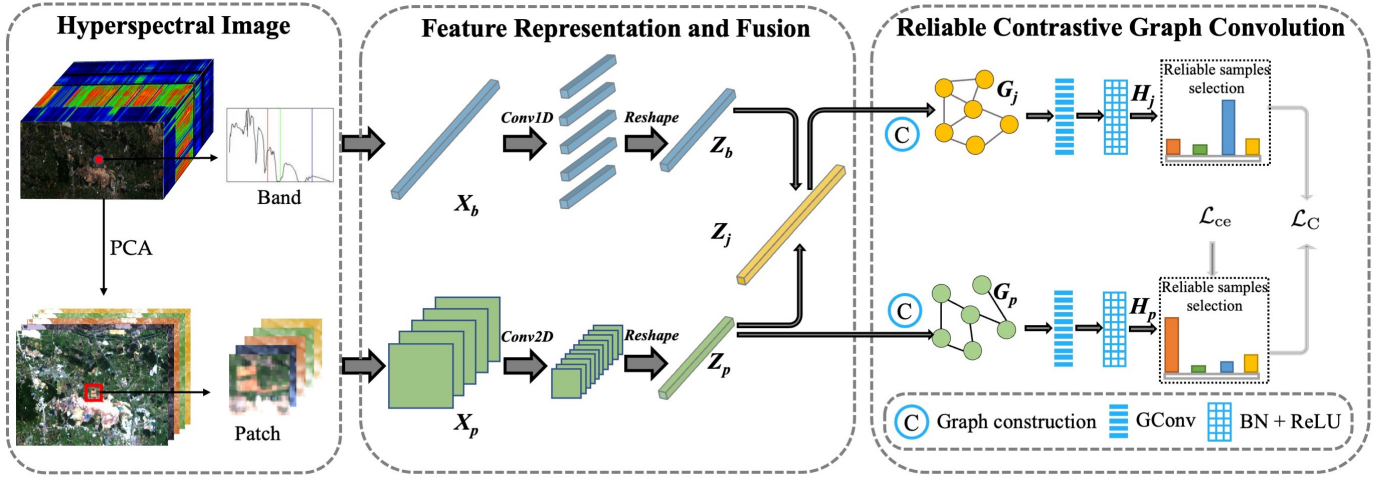


Fig. 1. Architecture of the proposed S^2RC -GCN. The model comprises three main components. Initially, it acquires the spatial and spectral features of the HSI, followed by utilizing 1D-CNN and 2D-CNN for feature extraction and fusion. Lastly, spatial features and the fused representation are employed for composition and reliable contrastive learning.

GCN: HSI can be represented as a graph $G = (V, E, X)$, where $V = \{v_i\}_{i=1,2,\dots}$ represents the set of pixels, N denotes the number of nodes, E is the set of concatenated edges, and $X \in \mathbb{R}^{N \times F}$ is the feature matrix containing attribute vectors for each node. $A \in \mathbb{R}^{N \times N}$ represents the corresponding adjacency matrix of the network, where $A_{ij} = 1$ if there is a concatenated edge between nodes v_i and v_j , otherwise $A_{ij} = 0$. $D \in \text{diag}(d_1, d_2, d_3, \dots, d_i)$ represents the corresponding degree matrix of the graph G , where $d_i = \sum_{j=1}^N A_{ij}$.

GCN extend traditional CNN to the graph domain, currently categorized into two types: null-domain GCNs and frequency-domain GCNs. This paper predominantly adopts frequency-domain GCNs, specifically the conventional type of GCN. We utilize frequency-domain GCNs to define the convolution operation by decomposing the graph signal in the frequency domain and then applying a spectral filter to the frequency domain components. The layer-by-layer propagation rule for graph convolution can be expressed as follows:

$$H^{(l+1)} = \sigma(\tilde{D}^{-\frac{1}{2}} \tilde{A} \tilde{D}^{-\frac{1}{2}} H^{(l)} W^{(l)}) \quad (1)$$

where $\tilde{A} = A + I_N$ represents the adjacency matrix of the added self-looped undirected graph G derived from the original adjacency matrix, and I_N is the unit matrix. The output matrix of layer l is denoted as $h^{(l)}$, with $H^{(0)} = X$ and $l = 0, 1, \dots, L - 1$ indicating the number of convolutional layers. $w^{(l)}$ refers to the trainable weight matrix for a specific layer. The activation function $\sigma(\cdot)$ exemplifies ReLU in the experiments.

B. Joint Spatial-Spectral Feature Extraction

Adjacent pixels are often associated with the same class in the HSI. Existing methods typically employ a 2D-CNN to extract features from patches. However, this approach may lead to a reduction in the contribution of spectral information to the central region of the image, resulting in reduced

robustness against noisy samples. To address this issue, we introduced a 1D-CNN into the network to fully leverage the spectral information of the HSI. The 1D-CNN extracts spectral features from bands, whereas the 2D-CNN extracts spatial-spectral features from patches. These two sets of features are concatenated to create a more resilient joint spatial-spectral features representation. To suppress the influence of useless information, we designed a SE-ResNet network that forced the model to focus on the feature information of useful channels, the details of which can be found in Section II-A.

X_b and X_p represent the spectral and spatial data of the HSI, respectively, where $X_b \in \mathbb{R}^{d \times N}$, d denotes the dimension of the samples. Additionally, a square with side length w is used to capture the spatial features around each pixel. The spectral dimension is reduced to p using PCA to obtain the initial spatial data $X_p \in \mathbb{R}^{d \times w \times w \times N}$. Next, we process X_b with the 1D-CNN to obtain the spectral feature $Z_b \in \mathbb{R}^{l_b \times N}$, where l_b represents the length of features. Simultaneously, we use the 2D-CNN to obtain the spatial feature Z_p . The encoding operations are defined as follows:

$$\begin{cases} Z_b = f_b(X_b) \in \mathbb{R}^{l_b \times N} \\ Z_p = f_p(X_p) \in \mathbb{R}^{l_p \times w_1 \times w_1 \times N}, \end{cases} \quad (2)$$

where $f_b(\cdot)$ and $f_p(\cdot)$ denote the mapping operations of the 1D-CNN and 2D-CNN, respectively. Because feature Z_p is a three-dimensional array, we flattened it to obtain a feature vector of length l_p as well as a new feature representation, $Z_p \in \mathbb{R}^{n \times l_p}$. Finally, we concatenate Z_p and Z_b to obtain the joint spatial-spectral feature $Z_j \in \mathbb{R}^{n \times l}$, where $l = l_b + l_p$.

C. Graph Construction

Traditionally, the use of shallow features of HSI to construct graphs is not robust and cannot be updated through the learning process. In this study, we used the spatial feature Z_p and spatial-spectral joint feature Z_j to construct the nodes of the

graphs. Edges are defined as potential interactions between two nodes, with the assumption that nodes with smaller distances are more likely to interact. As a node represents a spatial region in the original HSI, the constructed graph represents the spatial correlation between different regions of the image. The Euclidean distance defined in Eq. (3) is used. First, the correlation $dis(z^i, z^j)$ between all nodes is calculated to obtain the distance matrix $Dis \in \mathbb{R}^{N \times N}$.

$$Dis(Z) = \sqrt{\sum_{i=1}^N \sum_{j=1}^N (z^i - z^j)^2}. \quad (3)$$

Then, the K nodes closest to each node are selected as neighbors, and edges are generated between these nodes to obtain the structure of the graph. The adjacency matrix $A \in \mathbb{R}^{N \times N}$ is defined as:

$$A_{ij} = \begin{cases} 1, & z^i \in \mathcal{N}_k(z_j) \text{ or } z^j \in \mathcal{N}_k(z_i) \\ 0, & \text{Otherwise} \end{cases}. \quad (4)$$

where $\mathcal{N}_k(z_i)$ represents the set of neighbors. Through the above process, we input spatial features Z_p and joint features Z_j to obtain their adjacency matrices A_p and A_j , respectively. Combining the features and their corresponding adjacency matrices we obtain two graphs, $G_p = (Z_p, A_p)$ and $G_j = (Z_j, A_j)$. These two graphs then flow into two branches, and are processed using a graph convolution module. The mathematical description of this step is as follows:

$$\begin{cases} G'_p = \text{GConv}(G_p) + w_p \\ G'_j = \text{GConv}(G_j) + w_j \end{cases} \quad (5)$$

where $\text{GConv}(\cdot)$ and w represent the graph convolution operation and corresponding bias, respectively. The resulting G'_p and G'_j are then fed into the BN+ReLU module, generating nonlinear graph features G''_p and G''_j as follows:

$$\begin{cases} G''_p = \text{ReLU}(\text{BN}(G'_p)) \\ G''_j = \text{ReLU}(\text{BN}(G'_j)) \end{cases} \quad (6)$$

Finally, we obtain graph features notated H_j and H_p that aggregate neighbor information.

D. Reliable Contrastive GCN

Supervised contrastive loss provides rich supervisory information for contrastive learning using only unlabeled samples, assisting the model in learning better node representations and further improving model performance. During the learning process, an evaluation function is employed to measure the similarity of node encoding features. The goal is to maximize the similarity between nodes of the same category while minimizing the similarity between nodes of different categories, guiding the learning process.

Existing contrastive learning methods often use data augmentation to construct positive and negative sample pairs, but the augmentation process is prone to introducing noise. Therefore, this paper utilizes spatial feature H_p and spatial-spectral feature H_j for contrastive learning. Both features are extracted from hyperspectral data, avoiding the noise

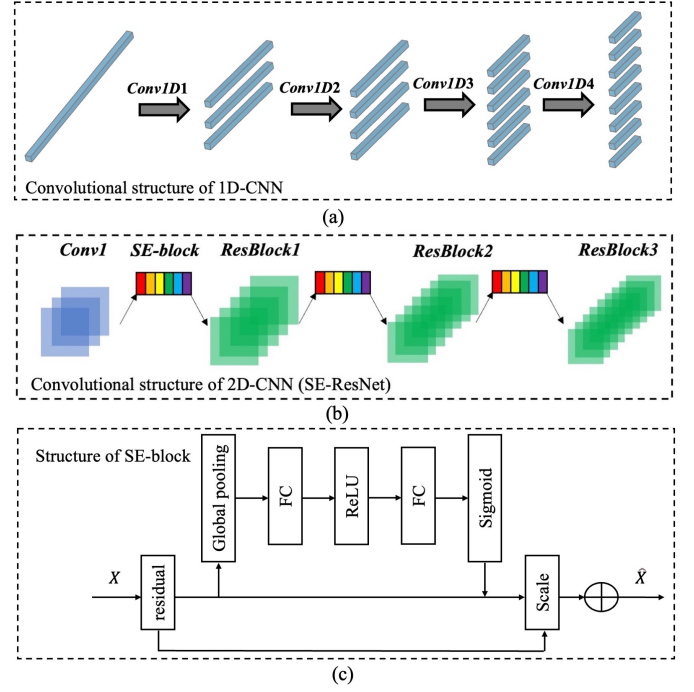


Fig. 2. Structural diagram of 1D-CNN and 2D-CNN, which also includes a detailed construction of the Squeeze-and-Excitation module. (a) 1D-CNN; (b) 2D-CNN; (c) SE-block

introduced by the data augmentation process. Assuming x^i is a labeled node, so h_j^i and h_p^i are the corresponding spatial and joint features, respectively. The positive example is a labeled node in the spatial feature with the same class, and the negative example is a labeled node with a different class.

To increase the quantity of positive and negative sample pairs while ensuring the reliability of contrastive learning, this paper employs a one-layer perceptron to output the classification probability before constructing sample pairs. If the probability is greater than a certain threshold, it is included in the labeled set. Therefore, we make full use of scarce but valuable labeled samples, using supervised contrastive loss to provide additional supervisory signals for learning node representations. The supervised contrastive loss is expressed as follows:

$$\ell(h_j^i, h_p^i) = -\lg \left[\frac{\sum_{m=1}^M 1_{[y^i = \phi(y^m)]} \exp(h_j^i, h_p^m)}{\sum_{m=1}^M (1_{[y^i = \phi(y^m)]} \exp(h_j^i, h_p^m) + 1_{[y^i \neq \phi(y^m)]} \exp(h_j^i, h_p^m))} \right], \quad (7)$$

where $1_{i \neq m} = \{0, 1\}$ is an indicator function. $\phi(y^m) = \{y^i = y^m \text{ or } y^i = f(h^m)\}$, where $f(h^m)$ represents obtaining the predicted label of h^m and M is the number of the set $\phi(y^m)$. There are two critical parameters in this algorithm. One is the threshold for label prediction, which is set to 0.99 in this article to ensure label reliability. The other is the temperature coefficient in contrastive learning, which is consistently set to 1 in all experiments. The overall objective for minimizing is the average of Eq. (7) for all given positive

TABLE I
CLASSIFICATION RESULTS (OA/NMI/KAPPA) OF VARIOUS METHODS ON JIANG XIA DATASETS. THE BEST RESULTS ARE SHOWN IN BOLD.

Class No.	1D-CNN	2D-CNN	3D-CNN	ResCapsNet	FuNet	SAGE-A	MDGCN	F ² HNN	Ours
1	59.47 ± 2.11	63.16 ± 0.52	75.51 ± 0.72	76.35 ± 0.56	80.59 ± 0.14	80.96 ± 1.12	89.58 ± 1.32	90.18 ± 0.72	88.27 ± 1.28
2	77.35 ± 1.28	82.44 ± 0.89	85.29 ± 1.41	91.42 ± 0.54	88.07 ± 0.42	73.16 ± 0.74	75.57 ± 0.51	90.70 ± 0.58	97.04 ± 0.79
3	95.87 ± 1.01	98.92 ± 0.23	94.23 ± 1.08	100.0 ± 0.00	99.35 ± 0.11	75.32 ± 0.87	84.51 ± 2.75	95.19 ± 0.21	93.42 ± 0.85
4	94.61 ± 1.89	95.96 ± 1.41	91.03 ± 0.69	95.76 ± 0.27	96.88 ± 0.57	82.88 ± 0.74	93.54 ± 2.68	86.25 ± 0.46	92.26 ± 0.72
5	71.02 ± 0.22	61.61 ± 0.57	72.09 ± 1.77	55.92 ± 0.80	46.94 ± 0.78	45.52 ± 0.28	71.48 ± 0.45	50.73 ± 0.55	75.24 ± 1.20
6	80.66 ± 0.17	74.22 ± 0.83	76.72 ± 0.94	85.24 ± 1.26	68.93 ± 0.87	66.54 ± 0.81	73.83 ± 1.66	70.48 ± 0.26	88.21 ± 0.81
7	73.59 ± 1.33	71.56 ± 0.45	75.20 ± 0.47	76.44 ± 0.75	76.23 ± 0.92	54.41 ± 0.43	81.50 ± 3.05	72.89 ± 0.88	82.77 ± 0.42
OA	79.59 ± 1.79	80.44 ± 0.69	82.82 ± 0.53	82.80 ± 0.25	79.42 ± 0.77	83.43 ± 0.98	85.28 ± 1.08	79.19 ± 1.41	87.39 ± 1.24
AA	81.68 ± 0.33	78.39 ± 0.61	80.23 ± 0.68	81.35 ± 1.03	78.34 ± 0.79	80.90 ± 1.48	83.03 ± 1.26	78.26 ± 1.24	86.69 ± 0.88
Kappa	80.60 ± 0.28	76.84 ± 0.96	79.64 ± 0.72	79.69 ± 0.24	79.13 ± 0.41	81.71 ± 0.76	82.31 ± 1.07	75.31 ± 1.49	84.90 ± 1.74

pairs, which is given by the following expression:

$$\mathcal{L}_C = \frac{1}{2n} \sum_{i=1}^n [\ell(h_j^i, h_p^i) + \ell(h_p^i, h_j^i)]. \quad (8)$$

Next, the actual output of the network is measured against the true labels using the cross-entropy loss \mathcal{L}_{ce} , which signifies the difference between the predicted output and the actual labels. Combining the contrastive loss and the cross-entropy loss, the overall output of the network is obtained, and the overall objective loss function is expressed as follows:

$$\mathcal{L} = \mathcal{L}_C + \mathcal{L}_{ce}. \quad (9)$$

III. EXPERIMENTS

A. Datasets

In this experiment, to comprehensively assess model performance, the paper utilizes a diverse set of datasets, including the complex land cover dataset, Jiang Xia, Xin Jiang and a generalized hyperspectral datasets, Salinas for evaluation.

Jiang Xia dataset: captured by the GF-5 satellite, comprises 330 bands with a spatial resolution of 30 m [9]. It encompasses seven classes: surface-mined area, road, water, crop land, forest land, and construction land, totaling 121,303 samples. For this study, 200 samples from each class are selected for training, while the remaining samples are reserved for testing. We follow the spatially weakly dependent dataset of the literature [28] for our experiments.

Xin Jiang dataset: is captured by the GF-5 satellite, as is the Jiang Xia dataset. The images are for the Ili Kazakh Autonomous Prefecture in Xinjiang. We also use the spatially weakly dependent dataset of Xinjiang from literature [28] for testing.

Salinas dataset: captured by the AVIRIS sensor in 1992, exhibits dimensions of $512 \times 217 \times 224$ after processing, with 512×217 pixels and 224 bands. The Salinas dataset includes a total of 16 classes. For this study, 30 samples from each class are selected for training, and the remaining samples are earmarked for testing.

B. Experimental Setup

Compared Methods. To facilitate a comprehensive comparison of models, this paper selects nine deep learning models for evaluation. These comprise four CNN-based models: 1D-CNN [19], 2D-CNN [20], 3D-CNN [21], and ResCapsNet [28], and four GNN-based models: FuNet [42], F²HNN [63], graph sample and aggregate attention (SAGE-A) [64], and MDGCN [39]. Each of these models is computed with optimized parameters.

Evaluation Metrics. In this paper, we employ three assessment indicators: Overall Accuracy (OA), Average Accuracy (AA), and Kappa. These indicators range from 0 to 1, with larger values indicating superior model performance.

C. Quantitative Evaluation

Tables I-III present the test results of the Jiang Xia dataset, Xin Jiang dataset, and Salinas dataset, respectively, and bold is the best performance. The tables contain the prediction accuracy of each class and use OA, AA, and Kappa to evaluate the overall prediction standard. We objectively analyzed the advantages and disadvantages of the algorithm using a quantitative analysis. The results showed that the methods based on the CNN and GCN have their own merits in terms of performance. Overall, the 1D-CNN algorithm performs poorly because it is only based on spectral information. Methods such as CNN use the neighborhood blocks of image pixels as the input of the network and, to a certain extent, jointly utilize the spatial and spectral information of HSI.

By contrast, the overall classification accuracy of the S²RC-GCN proposed in this study was the highest, indicating its effectiveness in classifying complex scenes. The OA, AA, and Kappa of the model on the Jiang Xia dataset all reached their highest values, which are $87.39\% \pm 1.24\%$, $86.69\% \pm 0.88\%$ and $84.90\% \pm 1.74\%$, respectively; these values are 4.59%, 3.89%, and 5.21% higher than ResCapsNet, respectively. The model demonstrated $71.42\% \pm 0.56\%$, $68.98\% \pm 0.87\%$, and $65.02\% \pm 0.76\%$ accuracies, respectively in the Xin Jiang dataset. In terms of OA metrics, it outperforms the optimal models in CNN-based and GCN-based by 0.54% and 2.62%, respectively. This result shows that combining the feature information of the HSI with the spatial structure features can further improve classification performance. Despite the

TABLE II
CLASSIFICATION RESULTS (OA/NMI/KAPPA) OF VARIOUS METHODS ON XIN JIANG DATASETS. THE BEST RESULTS ARE SHOWN IN BOLD.

Class	1D-CNN	2D-CNN	3DCNN	ResCapsNet	FuNet	SAGE-A	MDGCN	F ² HNN	Ours
1	69.42 ± 1.37	69.62 ± 0.93	66.26 ± 0.37	77.66 ± 0.39	94.08 ± 0.71	91.87 ± 0.26	82.47 ± 0.93	92.19 ± 1.25	88.92 ± 0.37
2	58.83 ± 0.76	63.52 ± 0.94	87.47 ± 0.75	85.29 ± 0.58	87.42 ± 0.53	77.62 ± 0.38	83.50 ± 0.29	86.98 ± 0.86	88.20 ± 0.58
3	81.65 ± 0.27	90.61 ± 1.27	93.73 ± 0.89	96.27 ± 0.62	93.04 ± 1.27	93.59 ± 1.36	89.63 ± 0.87	94.12 ± 1.83	93.41 ± 1.28
4	40.25 ± 1.89	38.82 ± 0.48	30.15 ± 1.24	31.67 ± 0.74	25.49 ± 0.20	28.29 ± 1.31	19.60 ± 1.78	26.79 ± 0.54	27.75 ± 1.16
5	14.55 ± 0.73	16.57 ± 1.63	32.65 ± 0.31	28.85 ± 0.89	26.48 ± 0.49	29.75 ± 1.08	31.38 ± 0.96	28.44 ± 0.57	36.28 ± 1.69
6	73.26 ± 0.84	81.04 ± 0.86	83.64 ± 0.58	90.13 ± 0.41	86.38 ± 0.44	75.26 ± 0.25	80.27 ± 0.44	84.08 ± 0.71	85.65 ± 0.29
7	46.31 ± 1.49	49.61 ± 0.74	65.29 ± 0.38	65.61 ± 0.28	71.19 ± 1.12	73.84 ± 0.42	70.36 ± 0.86	72.24 ± 1.47	76.48 ± 0.90
OA	54.81 ± 0.74	58.50 ± 0.71	67.02 ± 0.70	70.88 ± 0.70	68.80 ± 0.34	65.60 ± 0.75	64.81 ± 0.89	68.47 ± 1.74	71.42 ± 0.56
F1-score	54.80 ± 0.91	58.46 ± 0.56	64.35 ± 0.21	66.27 ± 0.82	63.07 ± 0.98	64.07 ± 1.42	62.27 ± 0.43	64.56 ± 2.17	68.98 ± 0.87
Kappa	47.28 ± 0.41	51.54 ± 0.29	61.32 ± 0.44	62.32 ± 0.39	60.38 ± 0.44	61.38 ± 1.03	58.96 ± 0.64	63.59 ± 2.03	65.02 ± 0.76

TABLE III
CLASSIFICATION RESULTS (OA/NMI/KAPPA) OF VARIOUS METHODS ON SALINAS DATASETS. THE BEST RESULTS ARE SHOWN IN BOLD.

Class No.	1D-CNN	2D-CNN	3D-CNN	ResCapsNet	FuNet	SAGE-A	MDGCN	F ² HNN	Ours
1	48.81 ± 0.12	100.0 ± 0.00	88.45 ± 2.15	99.40 ± 0.42	99.34 ± 0.53	99.78 ± 0.21	99.98 ± 0.03	98.19 ± 1.03	100.0 ± 0.00
2	72.53 ± 1.13	65.97 ± 4.60	87.08 ± 3.67	99.46 ± 0.39	99.17 ± 0.21	100.0 ± 0.00	99.90 ± 0.28	96.52 ± 1.19	100.0 ± 0.00
3	67.15 ± 2.13	71.53 ± 3.19	80.03 ± 2.13	98.58 ± 1.42	96.54 ± 1.39	99.45 ± 0.35	99.80 ± 0.21	94.36 ± 2.13	100.0 ± 0.00
4	51.70 ± 1.89	93.24 ± 3.19	75.31 ± 5.42	99.70 ± 0.17	97.32 ± 0.27	100.0 ± 0.00	97.49 ± 2.16	99.18 ± 0.28	99.13 ± 0.46
5	86.93 ± 1.47	93.78 ± 1.01	90.15 ± 3.17	98.90 ± 1.01	98.75 ± 0.89	98.75 ± 1.17	97.96 ± 0.77	99.77 ± 0.31	93.23 ± 2.59
6	90.65 ± 2.01	89.74 ± 2.32	96.34 ± 2.38	99.57 ± 0.38	99.18 ± 0.27	89.72 ± 3.62	99.10 ± 1.67	100.0 ± 0.00	96.67 ± 1.37
7	60.91 ± 2.11	98.26 ± 1.64	71.79 ± 4.62	99.50 ± 0.42	98.67 ± 1.30	100.0 ± 0.00	98.18 ± 1.49	99.99 ± 0.01	99.29 ± 0.34
8	94.31 ± 0.89	81.98 ± 4.32	97.78 ± 1.14	75.59 ± 6.72	72.38 ± 3.98	85.25 ± 5.27	92.78 ± 4.61	87.79 ± 4.89	99.74 ± 0.13
9	40.42 ± 3.71	99.47 ± 0.51	64.31 ± 6.33	99.75 ± 0.19	97.29 ± 0.61	95.31 ± 2.41	100.0 ± 0.00	99.67 ± 0.33	92.98 ± 2.41
10	71.60 ± 1.69	75.21 ± 2.75	86.74 ± 3.26	94.29 ± 1.90	91.44 ± 1.64	97.18 ± 0.82	98.31 ± 1.29	96.53 ± 2.55	93.91 ± 1.19
11	77.73 ± 2.11	61.24 ± 2.68	83.02 ± 2.97	97.57 ± 0.91	96.82 ± 0.78	96.36 ± 1.42	99.39 ± 0.55	99.19 ± 0.21	99.76 ± 0.17
12	60.83 ± 2.57	79.98 ± 0.45	98.10 ± 0.57	99.99 ± 0.01	99.21 ± 0.32	99.75 ± 0.12	99.01 ± 0.78	93.78 ± 1.01	95.30 ± 0.99
13	95.87 ± 2.33	96.73 ± 1.66	96.83 ± 1.13	99.95 ± 0.05	97.29 ± 0.86	96.39 ± 2.28	97.59 ± 1.32	97.78 ± 1.14	90.15 ± 1.26
14	92.72 ± 5.91	91.50 ± 3.05	88.05 ± 3.55	98.57 ± 0.28	95.10 ± 1.73	99.93 ± 0.09	97.92 ± 1.72	98.71 ± 0.72	95.61 ± 2.88
15	63.65 ± 6.29	82.41 ± 5.67	88.90 ± 1.10	72.18 ± 4.97	76.33 ± 4.62	87.23 ± 3.77	95.71 ± 4.57	81.86 ± 5.26	97.26 ± 1.63
16	91.78 ± 3.19	96.89 ± 2.19	99.78 ± 0.19	98.45 ± 0.83	97.99 ± 0.61	98.47 ± 0.81	98.18 ± 2.92	98.99 ± 0.63	99.85 ± 0.06
OA	77.03 ± 1.26	80.14 ± 0.86	88.03 ± 1.26	90.35 ± 1.67	87.64 ± 0.83	92.82 ± 1.00	97.25 ± 0.87	92.67 ± 0.77	97.49 ± 1.14
AA	72.52 ± 1.41	86.99 ± 0.56	90.52 ± 1.41	95.72 ± 0.41	94.55 ± 0.57	96.12 ± 0.82	98.21 ± 0.30	95.69 ± 0.34	97.87 ± 0.85
Kappa	74.55 ± 2.07	76.52 ± 0.95	86.55 ± 2.07	89.26 ± 1.30	86.72 ± 1.01	93.26 ± 0.76	96.94 ± 0.96	92.06 ± 0.85	97.43 ± 0.79

difficulty of testing on a complex land cover classification dataset, our proposed model nonetheless performed favorably compared to the other models in terms of classification performance. This demonstrates that our model has strong robustness.

Table III illustrates the performance of each model on the generic hyperspectral dataset, showcasing that our model consistently achieves optimal results. Nevertheless, an interesting trend emerges where the CNN-based model outperforms the GCN-based model on the complex land cover classification dataset. In contrast, the phenomenon is reversed on the Salinas dataset. We speculate that this discrepancy arises due to the intricate nature of land cover datasets, necessitating models with enhanced feature mining capabilities. Given that our model integrates deep features and capitalizes on the strengths of the GCN model, the combination has been proven to be optimal for each dataset.

D. Classification Maps

To observe the classification effect of the S²RC-GCN method more intuitively, Figures 3 and 4 show the visual maps of different models for the Jiang Xia and Salinas, respectively.

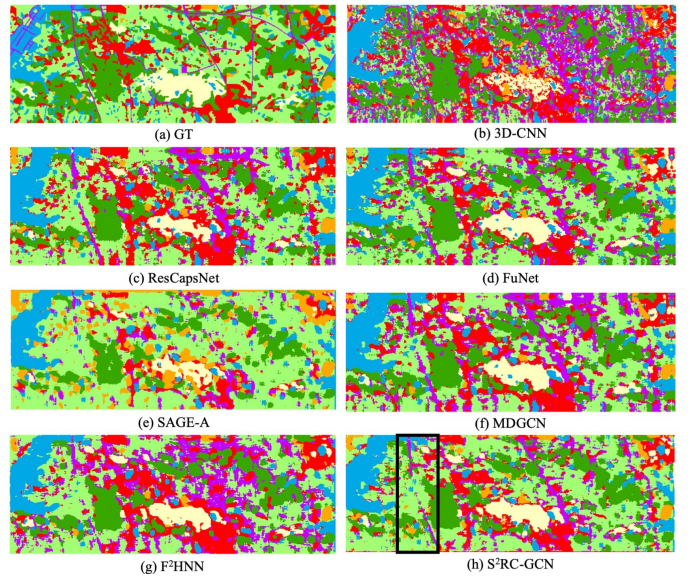


Fig. 3. The classification maps of different methods on the Jiang Xia dataset.

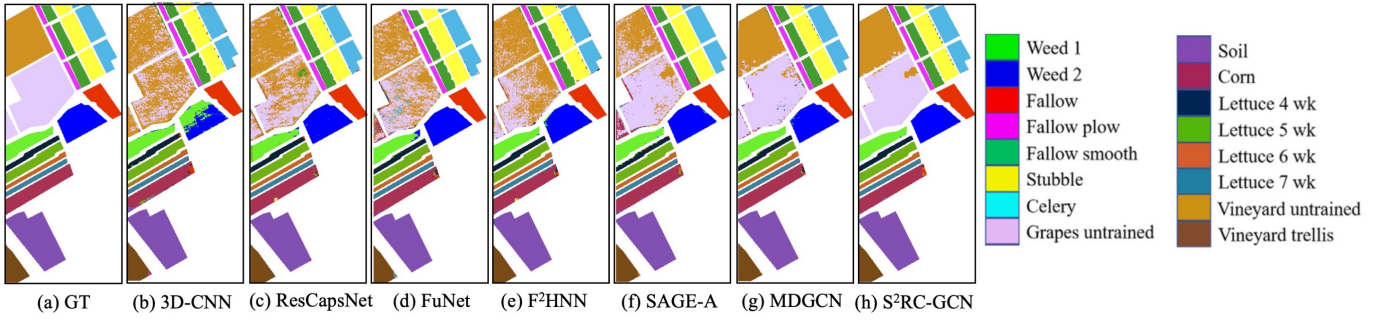


Fig. 4. The classification maps of different methods on the Salinas dataset.

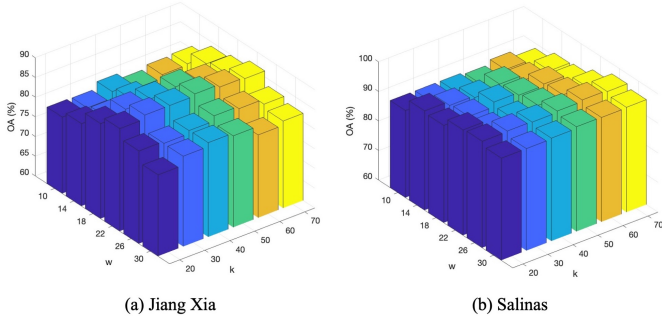


Fig. 5. Sensitivity to the k and w parameters on three datasets. k and w , respectively, represent the value of k -nearest neighbor composition and the input size.

We can see that the maps of the entire study area obtained by the S^2RC -GCN method had superior classification accuracy and visual robustness. As indicated by the black squares in Figure 3(h), the S^2RC -GCN model did not misclassify road areas as mineralized areas or bare land. S^2RC -GCN has a smoother classification, which more effectively divides the class boundaries of the mining area. In the overall classification of the Salinas, the S^2RC -GCN model exhibited a superior accuracy in the fine classification of grapes untrained and vineyard untrained.

In comparing the prediction results of the CNN-based and GCN-based algorithms for the entire image, these GCN-based methods have fewer misclassified points in the class boundary region. The remote sensing images of the two study areas have more complex ground-object distributions and spatial layout information. The fixed-structure CNN operator typically causes blurred edges, whereas the flexible-structure graph convolution operator is more suitable for pixel-level HSI classification.

E. Parameter Analysis

Figure 5 illustrates the impact of the number of neighbors k and the input size w on the OA across the Jiang Xia and Salinas datasets. Observing results, it becomes apparent that as w increases, the overall accuracy initially shows improvement. This is attributed to the fact that a too small input size can hin-

TABLE IV
ABLATION STUDY, WHERE (I) DEVOTES A VARIANT WITHOUT FUSION FEATURE; (II) DENOTES REPLACING SE-BLOCK INSIDE THE 2D-CNN; (III) DEVOTES A VARIANT THAT REMOVES THE RELIABLE CONTRASTIVE GRAPH CONVOLUTION MODULE.

Methods	Jiang Xia	Xin Jiang	Salinas
(I)	84.87 ± 1.28	69.44 ± 1.12	94.59 ± 1.28
(II)	86.93 ± 0.93	70.49 ± 0.62	96.93 ± 0.82
(III)	83.89 ± 0.81	70.23 ± 0.76	95.24 ± 0.94
Ours	87.39 ± 1.24	71.42 ± 0.56	97.49 ± 1.14

der the capture of surrounding spatial information. However, the model does not consistently exhibit an upward trend. Upon reaching a critical value, the model accuracy begins to decline, suggesting an excess capture of redundant information. The number of nearest neighbors, denoted as k , signifies the count of neighbors in the adjacency matrix for each node. The proposed model employs aggregated feature composition to construct a more accurate adjacency matrix, aiming to reduce connections between nodes of different classes. As k gradually increases, each node in the adjacency matrix incorporates more neighbors. However, these neighboring nodes may not belong to the same class as the focal node, and inputting this adjacency matrix into the GCN can impact classification outcomes. The figure demonstrates the model's resilience to changes in the value of k .

F. Ablation Study

In this section, we conduct extensive ablation experiments to verify the effectiveness of the proposed model. Specifically, we compare three variants of the S^2RC -GCN, (I) devotes a variant of our model that uses spectral and spatial features for contrastive learning rather than fusing features; (II) denotes replacing the attentional feature extraction module (SE-block) inside the 2D-CNN and using only regular ResNet to extract features; (III) devotes a variant of our model that removes the reliable contrastive graph convolution module. From the results in Table IV, we can draw the following conclusions:

(1) The joint feature obtained by integrating spectral and spatial features exhibit superior performance compared to the spatial features alone. This superiority arises from the higher feature similarity between the joint feature and the spatial

feature, aligning with the enhancement requirements in the comparison model and ensuring a strong connection between the two.

(2) The lack of the SE-block in the 2D-CNN will lead to a decrease in accuracy because the attention-based feature selection module can select more favorable features and filter the noisy information.

(2) By comparing our model with the results of (III), we can observe that the reliable contrastive graph convolution we proposed can reduce redundant information and improve the accuracy of the model. The omission of the attention mechanism led to reduced classification results, with an OA drop of 3.50%, 1.19%, and 1.85% for the three datasets, respectively.

IV. CONCLUSION

To improve the classification accuracy of HSI in complex backgrounds, this paper proposes a spatial-spectral reliable contrastive graph convolutional network named S²RC-GCN. S²RC-GCN uses 1D-CNN and 2D-CNN combined with SE attention module to extract important information to obtain spatial-spectral features. To make the joint feature more discriminative, this paper designs an adaptive group graph convolution module to improve the feature representation of the graph. In addition, we propose a reliable contrastive GCN, which uses nodes with true labels or predictive labels with high thresholds for contrastive learning to further learn more efficient graph representations. The experimental results show that S²RC-GCN can effectively improve the classification performance of complex remote sensing images. In future research, we will consider the multimodal features of HSI to further improve the classification accuracy of fine land cover.

V. ACKNOWLEDGMENT

This study was jointly supported by the Natural Science Foundation of China under Grants 42071430 and U21A2013, the Opening Fund of Key Laboratory of Geological Survey and Evaluation of Ministry of Education under Grant GLAB2022ZR02 and Grant GLAB2020ZR14.

Computation of this study was performed by the High-performance GPU Server (TX321203) Computing Centre of the National Education Field Equipment Renewal and Renovation Loan Financial Subsidy Project of China University of Geosciences, Wuhan.

REFERENCES

- [1] X. Liu, J. He, Y. Yao, J. Zhang, H. Liang, H. Wang, and Y. Hong, "Classifying urban land use by integrating remote sensing and social media data," *International Journal of Geographical Information Science*, vol. 31, no. 8, pp. 1675–1696, 2017.
- [2] X. Cheng and C. Zhang, "C2-yolo: Rotating object detection network for remote sensing images with complex backgrounds," in *2022 International Joint Conference on Neural Networks (IJCNN)*. IEEE, 2022, pp. 1–8.
- [3] P. Gong, J. Wang, L. Yu, Y. Zhao, Y. Zhao, L. Liang, Z. Niu, X. Huang, H. Fu, S. Liu *et al.*, "Finer resolution observation and monitoring of global land cover: First mapping results with landsat tm and etm+ data," *International Journal of Remote Sensing*, vol. 34, no. 7, pp. 2607–2654, 2013.
- [4] Y. Chen, Q. Yuan, Y. Tang, Y. Xiao, J. He, and L. Zhang, "Spirit: Spectral awareness interaction network with dynamic template for hyperspectral object tracking," *IEEE Transactions on Geoscience and Remote Sensing*, vol. 62, pp. 1–16, 2024.
- [5] S. Lai, L. Hu, J. Wang, L. Berti-Equille, and D. Wang, "Faithful vision-language interpretation via concept bottleneck models," in *The Twelfth International Conference on Learning Representations*, 2023.
- [6] S. Lai, X. Hu, H. Xu, Z. Ren, and Z. Liu, "Multimodal sentiment analysis: A survey," *Displays*, p. 102563, 2023.
- [7] S. Lai, X. Hu, J. Han, C. Wang, S. Mukhopadhyay, Z. Liu, and L. Ye, "Predicting lysine phosphoglycerylation sites using bidirectional encoder representations with transformers & protein feature extraction and selection," in *2022 15th International Congress on Image and Signal Processing, BioMedical Engineering and Informatics (CISP-BMEI)*. IEEE, 2022, pp. 1–6.
- [8] H. Xu, S. Lai, X. Li, and Y. Yang, "Cross-domain car detection model with integrated convolutional block attention mechanism," *Image and Vision Computing*, vol. 140, p. 104834, 2023.
- [9] W. Chen, S. Ouyang, J. Yang, X. Li, G. Zhou, and L. Wang, "Jagan: A framework for complex land cover classification using gaofen-5 ahsi images," *IEEE Journal of Selected Topics in Applied Earth Observations and Remote Sensing*, vol. 15, pp. 1591–1603, 2022.
- [10] Z. Chen, Z. Lu, H. Gao, Y. Zhang, J. Zhao, D. Hong, and B. Zhang, "Global to local: A hierarchical detection algorithm for hyperspectral image target detection," *IEEE Transactions on Geoscience and Remote Sensing*, vol. 60, pp. 1–15, 2022.
- [11] Z. Chen, G. Wu, H. Gao, Y. Ding, D. Hong, and B. Zhang, "Local aggregation and global attention network for hyperspectral image classification with spectral-induced aligned superpixel segmentation," *Expert Systems with Applications*, vol. 232, p. 120828, 2023.
- [12] Z. Chen, D. Hong, and H. Gao, "Grid network: Feature extraction in anisotropic perspective for hyperspectral image classification," *IEEE Geoscience and Remote Sensing Letters*, 2023.
- [13] Z. Chen, Y. Wang, H. Gao, Y. Ding, Q. Zhong, D. Hong, and B. Zhang, "Temporal difference-guided network for hyperspectral image change detection," *International Journal of Remote Sensing*, vol. 44, no. 19, pp. 6033–6059, 2023.
- [14] Y. Chen, Y. Tang, Z. Yin, T. Han, B. Zou, and H. Feng, "Single object tracking in satellite videos: A correlation filter-based dual-flow tracker," *IEEE Journal of Selected Topics in Applied Earth Observations and Remote Sensing*, vol. 15, pp. 6687–6698, 2022.
- [15] Y. Chen, Y. Tang, T. Han, Y. Zhang, B. Zou, and H. Feng, "Ramc: A rotation adaptive tracker with motion constraint for satellite video single-object tracking," *Remote Sensing*, vol. 14, no. 13, p. 3108, 2022.
- [16] R. Guan, Z. Li, X. Li, and C. Tang, "Pixel-superpixel contrastive learning and pseudo-label correction for hyperspectral image clustering," in *ICASSP 2024 - 2024 IEEE International Conference on Acoustics, Speech and Signal Processing (ICASSP)*, 2024, pp. 6795–6799.
- [17] K. Liang, L. Meng, M. Liu, Y. Liu, W. Tu, S. Wang, S. Zhou, X. Liu, and F. Sun, "Reasoning over different types of knowledge graphs: Static, temporal and multi-modal," *arXiv preprint arXiv:2212.05767*, 2022.
- [18] Y. Liu, H. Li, M. Gong, J. Liu, Y. Wu, M. Zhang, and J. Shi, "Evolutionary multitasking cnn architecture search for hyperspectral image classification," in *2022 International Joint Conference on Neural Networks (IJCNN)*. IEEE, 2022, pp. 01–08.
- [19] W. Hu, Y. Huang, L. Wei, F. Zhang, and H. Li, "Deep convolutional neural networks for hyperspectral image classification," *Journal of Sensors*, vol. 2015, pp. 1–12, 2015.
- [20] Y. Chen, H. Jiang, C. Li, X. Jia, and P. Ghamisi, "Deep feature extraction and classification of hyperspectral images based on convolutional neural networks," *IEEE transactions on geoscience and remote sensing*, vol. 54, no. 10, pp. 6232–6251, 2016.
- [21] Y. Li, H. Zhang, and Q. Shen, "Spectral-spatial classification of hyperspectral imagery with 3d convolutional neural network," *Remote Sensing*, vol. 9, no. 1, p. 67, 2017.
- [22] Q. Yan, T. Hu, Y. Sun, H. Tang, Y. Zhu, W. Dong, L. Van Gool, and Y. Zhang, "Towards high-quality hdr deghosting with conditional diffusion models," *IEEE Transactions on Circuits and Systems for Video Technology*, 2023.
- [23] B. Wang, T. Hu, B. Li, X. Chen, and Z. Zhang, "Gateor: A unified framework for gaze object prediction," in *Proceedings of the IEEE/CVF Conference on Computer Vision and Pattern Recognition*, 2022, pp. 19 588–19 597.

- [24] X. Zhang, T. Hu, J. He, and Q. Yan, "Efficient content reconstruction for high dynamic range imaging," in *ICASSP 2024 - 2024 IEEE International Conference on Acoustics, Speech and Signal Processing (ICASSP)*, 2024, pp. 7660–7664.
- [25] B. Rasti, P. Ghamisi, J. Plaza, and A. Plaza, "Fusion of hyperspectral and lidar data using sparse and low-rank component analysis," *IEEE Transactions on Geoscience and Remote Sensing*, vol. 55, no. 11, pp. 6354–6365, 2017.
- [26] Z. Zhong, J. Li, Z. Luo, and M. Chapman, "Spectral–spatial residual network for hyperspectral image classification: A 3-d deep learning framework," *IEEE Transactions on Geoscience and Remote Sensing*, vol. 56, no. 2, pp. 847–858, 2017.
- [27] W. Wang, S. Dou, Z. Jiang, and L. Sun, "A fast dense spectral–spatial convolution network framework for hyperspectral images classification," *Remote sensing*, vol. 10, no. 7, p. 1068, 2018.
- [28] R. Guan, Z. Li, T. Li, X. Li, J. Yang, and W. Chen, "Classification of heterogeneous mining areas based on rescapsnet and gaofen-5 imagery," *Remote Sensing*, vol. 14, no. 13, p. 3216, 2022.
- [29] Z. Chen and Y. Ge, "Occluded cloth-changing person re-identification," *arXiv preprint arXiv:2403.08557*, 2024.
- [30] Y. Ge, K. Niu, Z. Chen, and Q. Zhang, "Lightweight traffic sign recognition model based on dynamic feature extraction," in *International Conference on Applied Intelligence*. Springer, 2023, pp. 339–350.
- [31] Y. Ge, J. Zhang, Z. Chen, and B. Li, "End-to-end person search based on content awareness," in *2023 International Conference on Image Processing, Computer Vision and Machine Learning (ICICML)*. IEEE, 2023, pp. 1108–1111.
- [32] J. Zhang, Z. Chen, Y. Ge, and M. Yu, "An efficient convolutional multi-scale vision transformer for image classification," in *2023 International Conference on Image Processing, Computer Vision and Machine Learning (ICICML)*. IEEE, 2023, pp. 344–347.
- [33] Z. Chen, Y. Ge, J. Zhang, and X. Gao, "Multi-branch person re-identification net," in *2023 International Conference on Image Processing, Computer Vision and Machine Learning (ICICML)*. IEEE, 2023, pp. 1104–1107.
- [34] J. Liu, R. Guan, Z. Li, J. Zhang, Y. Hu, and X. Wang, "Adaptive multi-feature fusion graph convolutional network for hyperspectral image classification," *Remote Sensing*, vol. 15, no. 23, p. 5483, 2023.
- [35] M. Liu, Y. Liu, K. Liang, S. Wang, S. Zhou, and X. Liu, "Deep temporal graph clustering," *arXiv preprint arXiv:2305.10738*, 2023.
- [36] J. Wang, C. Tang, Z. Li, X. Liu, W. Zhang, E. Zhu, and L. Wang, "Hyperspectral band selection via region-aware latent features fusion based clustering," *Information Fusion*, vol. 79, pp. 162–173, 2022.
- [37] L. Ma, A. Ma, C. Ju, and X. Li, "Graph-based semi-supervised learning for spectral-spatial hyperspectral image classification," *pattern recognition letters*, vol. 83, pp. 133–142, 2016.
- [38] A. Qin, Z. Shang, J. Tian, Y. Wang, T. Zhang, and Y. Y. Tang, "Spectral–spatial graph convolutional networks for semisupervised hyperspectral image classification," *IEEE Geoscience and Remote Sensing Letters*, vol. 16, no. 2, pp. 241–245, 2018.
- [39] S. Wan, C. Gong, P. Zhong, B. Du, L. Zhang, and J. Yang, "Multiscale dynamic graph convolutional network for hyperspectral image classification," *IEEE Transactions on Geoscience and Remote Sensing*, vol. 58, no. 5, pp. 3162–3177, 2019.
- [40] R. Achanta, A. Shaji, K. Smith, A. Lucchi, P. Fua, and S. Süsstrunk, "Slic superpixels compared to state-of-the-art superpixel methods," *IEEE transactions on pattern analysis and machine intelligence*, vol. 34, no. 11, pp. 2274–2282, 2012.
- [41] Q. Liu, L. Xiao, J. Yang, and Z. Wei, "Cnn-enhanced graph convolutional network with pixel-and superpixel-level feature fusion for hyperspectral image classification," *IEEE Transactions on Geoscience and Remote Sensing*, vol. 59, no. 10, pp. 8657–8671, 2020.
- [42] D. Hong, L. Gao, J. Yao, B. Zhang, A. Plaza, and J. Chanussot, "Graph convolutional networks for hyperspectral image classification," *IEEE Transactions on Geoscience and Remote Sensing*, vol. 59, no. 7, pp. 5966–5978, 2021.
- [43] Z. Ma, Z. Jiang, and H. Zhang, "Hyperspectral image classification using feature fusion hypergraph convolution neural network," *IEEE Transactions on Geoscience and Remote Sensing*, vol. 60, pp. 1–14, 2021.
- [44] M. Zhang, H. Luo, W. Song, H. Mei, and C. Su, "Spectral-spatial offset graph convolutional networks for hyperspectral image classification," *Remote Sensing*, vol. 13, no. 21, p. 4342, 2021.
- [45] X. Huang, M. Dong, J. Li, and X. Guo, "A 3-d-swin transformer-based hierarchical contrastive learning method for hyperspectral image classification," *IEEE Transactions on Geoscience and Remote Sensing*, vol. 60, pp. 1–15, 2022.
- [46] T. Lu, Y. Hu, W. Fu, K. Ding, B. Bai, and L. Fang, "Scl-net: An end-to-end supervised contrastive learning network for hyperspectral image classification," *IEEE Transactions on Geoscience and Remote Sensing*, vol. 60, pp. 1–12, 2022.
- [47] R. Guan, Z. Li, W. Tu, J. Wang, Y. Liu, X. Li, C. Tang, and R. Feng, "Contrastive multi-view subspace clustering of hyperspectral images based on graph convolutional networks," *IEEE Transactions on Geoscience and Remote Sensing*, vol. 62, pp. 1–14, 2024.
- [48] W. Yu, S. Wan, G. Li, J. Yang, and C. Gong, "Hyperspectral image classification with contrastive graph convolutional network," *IEEE Transactions on Geoscience and Remote Sensing*, vol. 61, pp. 1–15, 2023.
- [49] X. Li, Z. Ni, and T. Zhang, "Mixture of personality improved spiking actor network for efficient multi-agent cooperation," *Frontiers in Neuroscience*, vol. 17, p. 1219405, 2023.
- [50] Z. Wang, Z. Zhang, J. Wang, C. Jiang, W. Wei, and Y. Ren, "Auv-assisted node repair for iout relying on multiagent reinforcement learning," *IEEE Internet of Things Journal*, vol. 11, no. 3, pp. 4139–4151, 2024.
- [51] X. Hou, J. Wang, C. Jiang, Z. Meng, J. Chen, and Y. Ren, "Efficient federated learning for metaverse via dynamic user selection, gradient quantization and resource allocation," *IEEE Journal on Selected Areas in Communications*, vol. 42, no. 4, pp. 850–866, 2024.
- [52] F. Shen, Y. Xie, J. Zhu, X. Zhu, and H. Zeng, "Git: Graph interactive transformer for vehicle re-identification," *IEEE Transactions on Image Processing*, 2023.
- [53] F. Shen, J. Zhu, X. Zhu, Y. Xie, and J. Huang, "Exploring spatial significance via hybrid pyramidal graph network for vehicle re-identification," *IEEE Transactions on Intelligent Transportation Systems*, vol. 23, no. 7, pp. 8793–8804, 2021.
- [54] Y. Xia, X. Shao, T. Ding, and J. Liu, "Prescribed intelligent elliptical pursuing by uavs: A reinforcement learning policy," *Expert Systems with Applications*, vol. 249, p. 123547, 2024.
- [55] Z. Wang, J. Du, C. Jiang, Z. Zhang, Y. Ren, and Z. Han, "Dynamic packet routing based on acoustic signal curve propagation in the auv-assisted iout," *IEEE Internet of Things Journal*, vol. 11, no. 6, pp. 9854–9869, 2024.
- [56] X. Hou, J. Wang, C. Jiang, X. Zhang, Y. Ren, and M. Debbah, "Uav-enabled covert federated learning," *IEEE Transactions on Wireless Communications*, vol. 22, no. 10, pp. 6793–6809, 2023.
- [57] F. Shen, X. Du, L. Zhang, and J. Tang, "Triplet contrastive learning for unsupervised vehicle re-identification," *arXiv preprint arXiv:2301.09498*, 2023.
- [58] F. Shen, X. Shu, X. Du, and J. Tang, "Pedestrian-specific bipartite-aware similarity learning for text-based person retrieval," in *Proceedings of the 31th ACM International Conference on Multimedia*, 2023.
- [59] F. Shen, J. Zhu, X. Zhu, J. Huang, H. Zeng, Z. Lei, and C. Cai, "An efficient multiresolution network for vehicle reidentification," *IEEE Internet of Things Journal*, vol. 9, no. 11, pp. 9049–9059, 2021.
- [60] R. Li, Y. Hu, L. Li, R. Guan, R. Yang, J. Zhan, W. Cai, Y. Wang, H. Xu, and L. Li, "Smwe-gfpnnet: A high-precision and robust method for forest fire smoke detection," *Knowledge-Based Systems*, vol. 289, p. 111528, 2024.
- [61] Z. Liu, R. Guan, J. Hu, W. Chen, and X. Li, "Remote sensing scene data generation using element geometric transformation and gan-based texture synthesis," *Applied Sciences*, vol. 12, no. 8, p. 3972, 2022.
- [62] C. Rodarmel and J. Shan, "Principal component analysis for hyperspectral image classification," *Surveying and Land Information Science*, vol. 62, no. 2, pp. 115–122, 2002.
- [63] Z. Ma, Z. Jiang, and H. Zhang, "Hyperspectral image classification using feature fusion hypergraph convolution neural network," *IEEE Transactions on Geoscience and Remote Sensing*, vol. 60, pp. 1–14, 2022.
- [64] Y. Ding, X. Zhao, Z. Zhang, W. Cai, and N. Yang, "Graph sample and aggregate-attention network for hyperspectral image classification," *IEEE Geoscience and Remote Sensing Letters*, vol. 19, pp. 1–5, 2022.